

# Impact of Thermally Driven Turbulence on the Bottom Melting of Ice

T. KEITZL, J. P. MELLADO, AND D. NOTZ

*Max Planck Institute for Meteorology, Hamburg, Germany*

(Manuscript received 8 July 2015, in final form 3 February 2016)

## ABSTRACT

Direct numerical simulation and laboratory experiments are used to investigate turbulent convection beneath a horizontal ice–water interface. Scaling laws are derived that quantify the dependence of the melt rate of the ice on the far-field temperature of the water under purely thermally driven conditions. The scaling laws, the simulations, and the laboratory experiments consistently yield that the melt rate increases by two orders of magnitude, from  $\approx 10^1$  to  $\approx 10^3$  mm day<sup>-1</sup>, as the far-field temperature increases from 4° to 8°C. The strong temperature dependence of the melt rate is explained by analyzing the vertical structure of the flow: For far-field temperatures below 8°C, the flow features a stably stratified, diffusive layer next to the ice that shields it from the warmer, turbulent outer layer. The stratification in the diffusive layer diminishes as the far-field temperature increases and vanishes for far-field temperatures far above 8°C. Possible implications of these results for ice–ocean interfaces are discussed. The drastic melt-rate increase implies that turbulence needs to be considered in the analysis of ice–water interfaces even in shear-free conditions.

## 1. Introduction

Horizontal ice–water interfaces are ubiquitous in polar regions. They are found at the bottom of ice shelves, sea ice, and lake ice. In regards to ice shelves, bottom ablation in the Antarctic has caused an increasing glacier flow speed and glacier mass loss to the ocean over recent decades (Wouters et al. 2015). In regards to sea ice, bottom ablation in the Arctic has increased substantially in recent years (Perovich et al. 2013). The exact rates of bottom ablation cannot always be reconstructed from observational records and uncertainties remain of order one (Notz et al. 2003). In particular, it is not yet well understood how the turbulent motion of water beneath these interfaces influences the internal-energy flux that ablates the ice at the bottom. Here, we investigate the influence of turbulence on rates of bottom ablation of ice with laboratory experiments and direct numerical simulations.

The evolution of the flow in natural systems with horizontal ice–water interfaces is determined by several processes: buoyancy forcing, shear forcing, the effect of solutes, and the influence of surface roughness and heterogeneity. Rather than trying to capture the impact

of all these processes on the interfacial internal-energy and salt fluxes, we here instead aim at simplifying the problem to its fundamental core. The simplified setup that we investigate is purely thermally driven free convection beneath a smooth fresh-ice–freshwater interface considering the density anomaly of the water.

However simple, our setup directly encompasses aspects of the flow underneath an ice–water interface from at least two more general systems: shear forcing and the effect of the solute salt. Shear forcing as well as buoyancy forcing create a similar vertical flow structure next to an interface (Pope 2000; Mellado 2012). Whenever turbulence aids the ablation of ice, a diffusive layer, however thin, forms between the ice and the turbulent layer irrespective of the forcing. A similar reasoning applies to the similarities between the present freshwater setup and a setup using seawater instead. With salt, the flow structure is qualitatively similar to the one induced by a thermally driven system. When ice is ablating on top of seawater, a lighter layer of almost freshwater resides aloft a denser layer of saline seawater. Nonlinear mixing of the layers can render a buoyancy reversal close to the interface. The resulting mean-buoyancy profile found beneath sea ice (Martin and Kauffman 1977) is similar to the mean-buoyancy profile that we focus on here, and we will discuss possible implications of our results of the fresh-ice–freshwater system for the more general case of ice floating on a salty ocean.

---

*Corresponding author address:* T. Keitzl, Max Planck Institute for Meteorology, Bundesstraße 53, 20146 Hamburg, Germany.  
E-mail: t@keitzl.com

Martin and Kauffman (1977) examine free convection beneath sea ice in the laboratory. They study the temporal evolution of temperature and salinity profiles beneath floating ice. In their experiment, the ice floats on warm and salty water that is initially at rest. They maintain a constant far-field temperature and run the experiment until it reaches a steady state. From their bounded laboratory configuration and a one-dimensional theoretical model, they find an enhancement of the melt rate by a constant factor of about 2.5 compared to purely diffusive energy exchange. Their finding is based on the boundary layer structure they observe: a diffusive layer next to the interface overlies a layer of double-diffusive convection followed by thermal convection in the far field.

An unbounded, quasi-steady, free-convection system (the counterpart to a bounded, steady-state laboratory experiment) is hard to measure to satisfactory resolution in the field or laboratory. Direct numerical simulation offers an opportunity to study detailed boundary layer structures for free-convection systems that do not feel any bounding geometry and do not involve any turbulence model. Mellado (2012) provides the boundary layer structure of purely buoyancy-driven free convection over a heated plate. He forces free convection with a linear buoyancy function; thus, this work does not account for buoyancy reversal. Further studies do account for buoyancy reversal, such as in the cloud-top mixing layer (Siems et al. 1990; Wunsch 2003; Mellado 2010). Unfortunately, these studies do not account for the effect of a solid surface as intrinsic to convection beneath ice. In this paper, we extend this previous work to include the effect of a solid surface next to a region of buoyancy reversal, as occurs in convection beneath ice.

This study considers the melting of ice on top of thermally driven free-convective water with laboratory experiments and with direct numerical simulations. We employ the laboratory experiments to ensure that the simulations capture all relevant aspects of the physics. We employ direct numerical simulations to overcome resolution and size limitations of the laboratory experiment and yield statistically converged boundary layer mean profiles. From both laboratory experiment and simulations we obtain melt rates and boundary layer mean profiles. Based on the observed boundary layer structure, its temporal evolution, and the underlying dynamic, we derive an analytical expression for the melt rate that explains laboratory and simulation results. We then discuss our results in the context of more general systems, investigating in particular the impact of melt-water advection on the flow, the spatial inhomogeneity of the melt rate, and estimating the effect of salinity on the derived melt rates. We conclude that the turbulent

enhancement of the melt rate of ice needs to be considered even in the absence of shear.

## 2. Setup and methods

A mass of solid, pure ice rests on top of an initially motionless body of pure water of fixed uniform temperature  $T_\infty$  (Fig. 1a). The ice mass is isothermal at the freezing temperature of water  $T_{\text{ice}}$  and has a smooth surface. Hence, the ice imposes a Dirichlet boundary condition on the temperature field of the water and a no-slip boundary condition on the velocity field of the water. We consider the ice–water interface together with the water body as our system of interest.

This system is purely buoyancy driven. We define buoyancy  $b$  as

$$b(T, T_\infty) = g \frac{\rho(T_\infty) - \rho(T)}{\rho(T_\infty)}, \quad (1)$$

with Earth's gravitational acceleration  $g$  and water density  $\rho(T)$ . Subsequently, we assume a second-order temperature dependence in the density

$$\rho(T) = \rho_m [1 - \beta(T - T_m)^2], \quad (2)$$

with the temperature of maximum density  $T_m = 3.98^\circ\text{C}$ ,  $\rho_m = 999.96 \text{ kg m}^{-3}$ , and a thermal expansion coefficient  $\beta = -7.00 \times 10^{-6} \text{ }^\circ\text{C}^{-2}$ . This second-order approximation yields a relative deviation from Eq. (6) of Sharqawy et al. (2010) of less than 0.01% between  $0^\circ$  and  $30^\circ\text{C}$ .

With increasing distance from the interface, the water temperature increases from  $T_{\text{ice}}$  at the interface to  $T_\infty$  in the far field (Fig. 1b). As the water temperature increases, the density first increases (as long as  $T < T_m$ ) and then decreases (when  $T > T_m$ ; Fig. 1c). Accordingly, the buoyancy first decreases and then increases again. Hence, for  $T_\infty > T_m$ , the buoyancy in the far field is higher than the buoyancy closer to the interface, and the system is convectively unstable (Fig. 1d). We are interested in this convectively unstable regime.

The temperature difference  $\Delta T_\infty = T_\infty - T_{\text{ice}}$  divides the system into two convective regimes based on  $\Delta T_m = T_m - T_{\text{ice}}$ . For  $\Delta T_\infty > 2\Delta T_m$ , the whole column of fluid can overturn (Fig. 1d, reddish profiles). In contrast, for  $\Delta T_\infty < 2\Delta T_m$ , there exists a layer next to the interface that is stably stratified (Fig. 1d, bluish profiles). This stably stratified layer beneath the ice acts as a shield against the warmer fluid of the convectively unstable region, as we will show below.

The spatiotemporal evolution of the system, given as velocity field  $\mathbf{v}(\mathbf{x}, t)$ , temperature field  $T(\mathbf{x}, t)$ , spatial coordinate  $\mathbf{x} = x_1\mathbf{e}_1 + x_2\mathbf{e}_2 + x_3\mathbf{e}_3$ ,  $\mathbf{e}_i = \varepsilon_{ijk}\mathbf{e}_j\mathbf{e}_k$ , and time

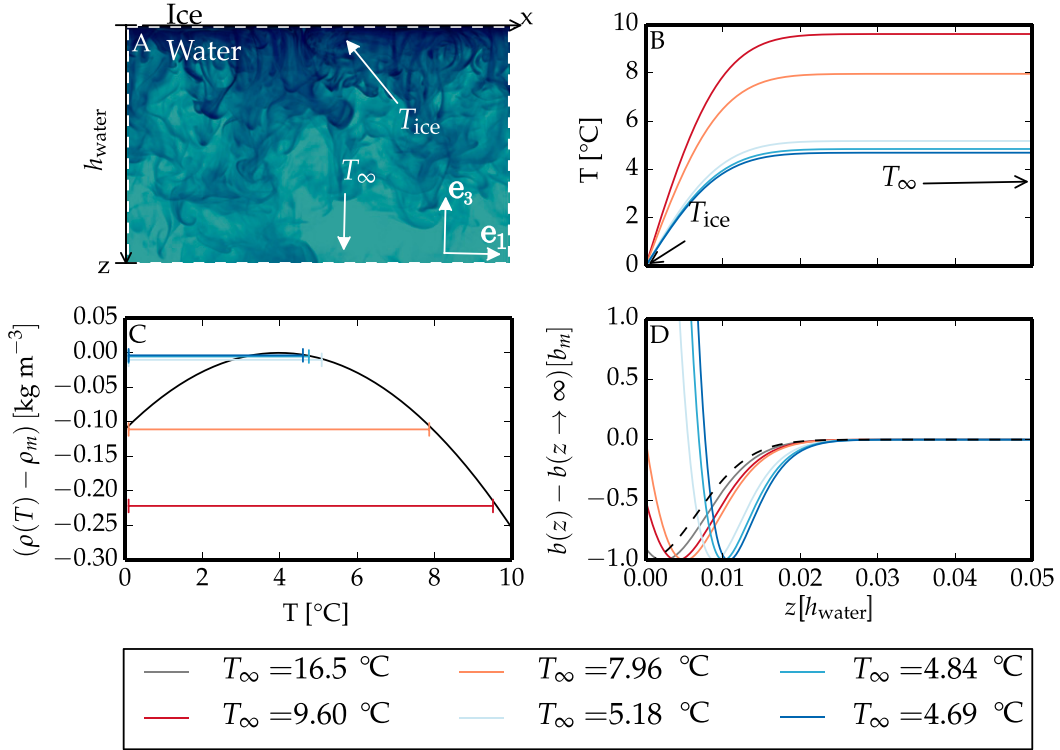


FIG. 1. Sketch of the system studied in this work. (a) Ice rests on top of a water body (greenish). We focus on the region limited by the white dashed line. A visualization of a turbulently mixed temperature field is exemplarily given (dark blue). (b) The water temperature increases from the interface value  $T_{\text{ice}}$  to the far-field value  $T_\infty$ . The distance from the interface is given in units of the tank height  $h_{\text{water}}$ . Different colors symbolize different far-field temperatures. The given profiles are the initial mean profiles of the numerical simulations. (c) Colored bars indicate the temperature range of density variation that characterizes the system for a certain far-field water temperature. (d) The resulting buoyancy profiles lead to convective instability.

$t$ , follows the evolution equations for mass, momentum, and internal energy:

$$\partial_t v_j = 0, \quad (3a)$$

$$\partial_t v_i = -v_j \partial_j v_i + \nu \partial_j^2 v_i - \partial_i p + b \delta_{i3}, \quad \text{and} \quad (3b)$$

$$\partial_t T = -v_j \partial_j T + \kappa \partial_j^2 T. \quad (3c)$$

We have given the equations in the Boussinesq approximation. The variable  $\nu$  is the kinematic viscosity,  $\kappa$  is the thermal diffusivity,  $p$  is the modified kinematic pressure,  $\partial_t$  is the temporal derivative, and  $\partial_i$  is the spatial derivative in direction  $\mathbf{e}_i$ .

The spatiotemporal evolution of the system is determined by the buoyancy  $b$  [Eq. (3b)]. For the analysis of the problem, it proves useful to express the dependence of the buoyancy on the temperature, given by Eq. (1), as

$$b = b_m (\theta/\theta_m) (2 - \theta/\theta_m). \quad (4)$$

The minimum buoyancy  $b_m$  is then given by

$$b_m = g \frac{\beta T_m^2}{\rho(T_\infty)} \frac{\theta_m^2}{(1 - \theta_m)^2}, \quad g \frac{\beta T_m^2}{\rho(T_\infty)} \approx -1.1 \times 10^{-4} \text{ m s}^{-2}. \quad (5)$$

The variable  $\theta$  is a normalized temperature

$$\theta(T, T_\infty) = \frac{T - T_\infty}{T_{\text{ice}} - T_\infty}, \quad (6)$$

which varies between 0 in the far field and 1 at the interface. For convectively unstable conditions,  $T_\infty > T_m$ , the far-field temperature parameter

$$\theta_m(T_\infty) = \theta(T = T_m, T_\infty) = \frac{T_m - T_\infty}{T_{\text{ice}} - T_\infty} \quad (7)$$

varies between 0 and 1. The far-field temperature parameter  $\theta_m$  denotes the fraction of the temperature range  $[T_{\text{ice}}, T_\infty]$  that locally stratifies the fluid unstably, and  $(1 - \theta_m)$  denotes the fraction that locally stratifies the fluid stably.

The flow develops freely into the far field and does not feel any solid boundary but the ice–water interface. For

sufficiently low viscosity, the system becomes turbulent, decorrelates from its initial state after a sufficiently long time, and depends solely on the set of control parameters  $\{\nu, \kappa, b_m, \theta_m\}$ . Dimensional analysis provides the set of independent control parameters  $\{\text{Pr}, \theta_m\}$ , with  $\text{Pr} = \nu/\kappa$ . Here, we chose to nondimensionalize the system by  $b_m$  instead of by the full buoyancy difference across the system because  $b_m$  gives the convective instability driving the flow. We constrain this investigation to waterlike fluids of the fixed Prandtl number  $\text{Pr} = 10$ . Hence, any flow property solely depends on the governing parameter  $\theta_m$  and on the position in space and time  $\{\theta_m, \mathbf{x}, t\}$ . The fully developed turbulent system is statistically homogeneous in horizontal directions. We denote horizontally averaged quantities by  $\langle \cdot \rangle$  and fluctuations around that mean by a prime. Horizontally averaged statistics only depend on  $\{\theta_m, z, t\}$  with  $z = -\mathbf{x}\mathbf{e}_3$  and the origin of  $\mathbf{x}$  chosen such that  $z$  gives the distance from the interface. The terms  $\theta_m, b_m$ , and  $T_\infty$  equivalently describe the system [Eqs. (5) and (7)].

#### a. Laboratory experiment

The laboratory setup that mimics the system consists of a Plexiglas tank filled with tap water, a thermistor cascade just beneath the water surface, and an ice block dangling on a manual tackle just above the water surface. The setup resides in a cold room whose temperature can be controlled with a precision of  $\pm 3^\circ\text{C}$ . The water body has the dimensions  $(0.347\text{ m})^3$  and is laterally isolated by a Styrofoam cover around the tank. The height of the water tank is  $h_{\text{water}} = 0.347\text{ m}$ . Temperature changes are measured with a cascade of 23 thermistors. The cascade has a spacing of 7 mm between the thermistors and a total profile length of 154 mm. Each thermistor is spherical with a radius of 1 mm and is placed on the tip of a 4-mm-thick and 2-cm-long finger to minimize the influence of the instrument body on the flow. The precision of the temperature measurement is at least 0.01 K, while temperature changes are measured with a response time of 2 to 4 s depending on the sign of the temperature change. The ice block, 8- to 13-cm thick, covers almost the entire water surface and is prepared from distilled water prior to the experiment.

Before an experiment is conducted, we orientate the system components and prepare the temperatures of the water body and the cold room. We level the ice block such that its surface can be attached evenly to the water surface, and we displace the thermistor cascade such that the upper thermistor is just beneath the water surface. A pump mixes the water body to a homogenous initial temperature  $T_\infty$ . The cold-room temperature matches  $T_\infty$  to minimize any temperature gradient between the water body and its lateral surrounding. We

keep the cold-room temperature constant at  $T_\infty$  for several hours to ensure that the ice is isothermal. The melting of the ice due to its exposure to the cold-room air is little compared to the melting due to its exposure to the water body later on. When the pump stops, we await the decay of turbulence kinetic energy for 3 min and cautiously lower the ice block via the manual tackle.

The experiment starts as soon as the ice touches the water surface. The ice is not lowered further. The thermistor cascade measures a temperature profile every 5 s during the experiment run time  $t_{\text{run}}$ . After that, the ice block is lifted from the water surface and the recording continues for a short while as the water is mixed with the pump to record the final mean temperature of the system  $T_{\text{end}}$ . This entire procedure constitutes one realization of the laboratory experiment. The horizontal position of the thermistor cascade is different in each laboratory realization.

First, we focus on the setup of  $T_\infty = 5^\circ\text{C}$  because considerably higher and lower far-field temperatures handicap the measurement. For higher far-field temperatures, the system evolves too quickly compared to the response time of the thermistors. For lower far-field temperatures, the expected temperature change in the far field is too little compared to the signal-to-noise ratio. We record an ensemble of 25 realizations at  $T_\infty = 5^\circ\text{C}$  and  $t_{\text{run}} = 15\text{ min}$  to capture the mean-temperature profile of the turbulent system. Second, we record several ensembles of small realization number (three to five) at  $T_\infty \in \{4.5, 5, 6, 14.8\}^\circ\text{C}$  and varying  $t_{\text{run}}$  to capture the temporal bulk temperature change of the turbulent system.

#### b. Direct numerical simulation

We integrate Eqs. (3) using a high-order, finite-difference method on a collocated, structured grid. We approximate the integration by a fourth-order Runge–Kutta scheme and the spatial derivatives by sixth-order, spectral-like finite differences (Williamson 1980; Lele 1992). After every integration step, a pressure solver ensures fulfillment of the solenoidal constraint. For this we use a Fourier decomposition along periodic horizontal coordinates and a factorization of the resulting second-order equations in the vertical coordinate (Mellado and Ansgore 2012).

The calculations are performed on a grid of 576 grid points in the vertical direction and 1280 grid points in both horizontal directions. Adequacy of vertical resolution, domain height, and domain width has been assured so that the results discussed in this paper are sufficiently independent of those simulation properties. The grid spacing is uniform in the horizontal directions and in most of the vertical direction. The resolution in the vertical direction close to the interface, however, is

TABLE 1. Properties of the numerical simulations. Far-field temperature parameter  $\theta_m$ , far-field temperature  $T_\infty$ , magnitude of minimum buoyancy  $|b_m|$ , and Richardson number  $Ri_0$  equivalently define the simulation [Eqs. (5), (7), and (26)] and are given for the reader's convenience. The diffusive length scale  $z_0$  is defined in Eq. (15). The boundary layer height  $z_*$  and the convective velocity scale  $w_*$  are defined in Eqs. (16) and (17), respectively. The turbulent Reynolds number  $Re_{\text{turb}}$  is the maximum value of  $e^2/(\epsilon\nu)$  in the domain with turbulence kinetic energy  $e$ , viscous dissipation rate  $\epsilon$ , and viscosity  $\nu$ . The terms  $Re_{\text{turb}}$  and  $w_*z_*/\nu^{-1}$  are measures for the scale separation in the simulations;  $\eta$  is the domainwide minimum Kolmogorov scale. The diffusive velocity scale is  $w_0 = (z_0 b_m)^{1/2}$ . The melt rate is given with Eq. (21). Columns 6–10 are evaluated at the final time step of the simulations. The grid size of the simulations is  $1280 \times 576 \times 1280$ .

$\theta_m$	$T_\infty$ (°C)	$ b_m $ ( $\text{m s}^{-2}$ )	$Ri_0$	$z_0$ (mm)	$z_*$ (m)	$w_*z_*/\nu^{-1}$	$Re_{\text{turb}}$	$\eta$ (mm)	$w_{\text{rms}}^{\text{max}}/w_0$	$w_f$ ( $\text{mm day}^{-1}$ )
0.152	4.69	$3.6 \times 10^{-5}$	31	39	1.05	950	190	5.6	0.81	42
0.179 <sup>a</sup>	4.85	$0.5 \times 10^{-4}$	21	31	2.56	3600	950	3.8	1.27	58
0.232	5.18	$1.0 \times 10^{-4}$	11	21	0.86	1100	200	3.4	0.95	90
0.500	7.96	$1.1 \times 10^{-3}$	1	5.6	0.37	900	140	1.6	1.03	400
0.586	9.61	$2.2 \times 10^{-3}$	0.5	4.0	0.29	820	120	1.3	1.01	610
0.760	16.57	$1.1 \times 10^{-2}$	0.1	2.0	0.15	670	87	0.8	0.94	1700
1.000	$T_\infty$	$b_m(T_\infty)$	0	—	—	531	34	—	—	$w_f(T_\infty)$
0.500 <sup>b</sup>	7.96	$1.1 \times 10^{-3}$	1	5.6	0.39	960	140	1.5	1.04	390
0.841 <sup>b,c</sup>	25.00	$3.1 \times 10^{-2}$	0.04	1.3	0.14	850	88	0.5	0.99	3200
0.901 <sup>b,c</sup>	40.00	$0.9 \times 10^{-1}$	0.01	0.9	0.12	1000	85	0.4	1.01	6700

<sup>a</sup> A simulation of extended size  $2560 \times 1088 \times 2560$ .

<sup>b</sup> Simulations with background mean advection.

<sup>c</sup> Simulations of size  $512 \times 576 \times 512$ .

increased because the main mean-temperature variation all over the domain occurs close to the interface. This temperature variation potentially entails the main mean-buoyancy change, a change in the forcing of the system from a positive to the global-extreme negative value and back to almost zero (Fig. 1d). To fully cover this buoyancy variation, we increase the resolution next to the interface by a factor of 5. The regions of uniform and adjusted resolution along the vertical direction are gradually matched by hyperbolic tangents. Finally, the grid in the vertical direction far from the interface is coarsened to save computing time. This part of the domain serves to diminish the influence of the computational boundary on the flow.

The boundary conditions in the velocity field are no-slip and no-penetration at the interface and free-slip and no-penetration in the far field. The boundary conditions in the temperature field are Dirichlet at the interface and Neumann in the far field. The initial condition in the temperature field is an error function of thickness  $d$  and zero in the velocity field. The temperature field is perturbed close to the interface with a wavelength that corresponds to  $7d$  [see Mellado (2012) for details].

We simulate systems of different far-field temperatures  $T_\infty$  (Table 1). We study the system of  $\Delta T_\infty = 2\Delta T_m$  ( $\theta_m = 0.5$ ) and three systems of both higher and lower buoyancy at the interface. The simulation of  $\theta_m = 0.179$  is done on an extended grid of size  $2560 \times 1088 \times 2560$  to reach higher Reynolds numbers, to increase the statistical convergence, and to calculate the melt rate more accurately. In addition, we perform three numerical

simulations with altered flow boundary conditions to study the influence of meltwater on the flow.

The final boundary layer height of the simulated systems  $z_*$  varies between 0.12 and 1.05 m. The simulations reach Reynolds numbers  $w_*z_*/\nu$  and  $e^2/(\epsilon\nu)$  of up to 3600 and 1000, respectively, with the turbulence kinetic energy  $e$ , the viscous dissipation rate  $\epsilon$ , the convective velocity scale  $w_*$ , and the viscosity  $\nu$ .

### 3. Similarity of laboratory experiment and numerical simulation

We compare an ensemble of 25 laboratory realizations of  $T_\infty = (5.00 \pm 0.01)^\circ\text{C}$  to one simulation of  $T_\infty = 4.98^\circ\text{C}$  ( $\theta_m = 0.20$ ). The simulation grid needed to resemble a laboratory tank of domain size 0.360 m is just  $1024 \times 384 \times 1024$  grid points, where we choose an aspect ratio of eight to one instead of one to one. Within a horizontal cross section of  $1024 \times 1024$  grid points, we choose 256 equally distributed base locations to obtain tower data measurements. The tower data consist of the temporal evolution of the vertical temperature profile beneath the ice interface, just as a laboratory realization does. We qualitatively compare the phenomenology obtained from simulation visualizations and laboratory realizations with dyed ice, and we quantitatively compare the temporal evolution of both the mean behavior and individual tower data of the simulation and the laboratory experiment.

Qualitatively, the structure of the boundary layer beneath the ice in the laboratory matches the one in the

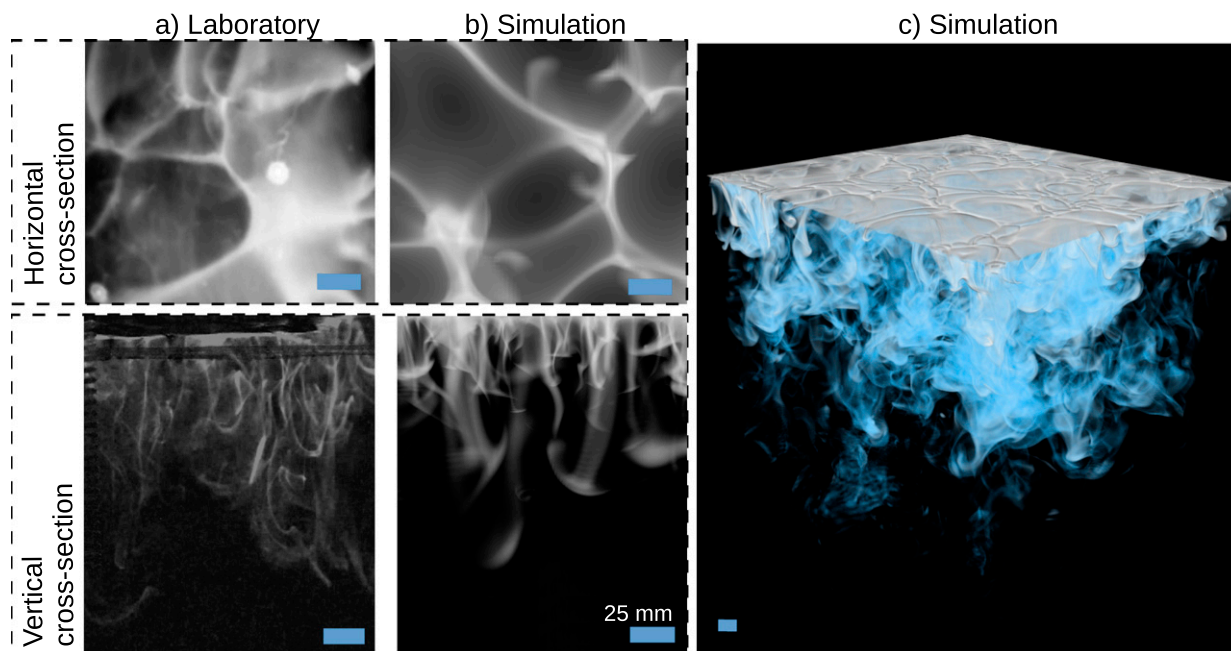


FIG. 2. Structure of the flow as retrieved from a laboratory tank (a) experiment and (b), (c) simulation. Bright fluid indicates a low temperature compared to the temperature of the dark warmer surrounding fluid. The blue dash indicates a length of 25 mm. Dashed boxes contain a horizontal cross section (upper box) and a vertical cross section (lower box). A visualization of the temporal evolution of (c) can be found in Keitzl et al. (2014). Note that the laboratory tank experiment visualizes a substituting setup in which—for visualization purposes—a constant temperature cooling plate is used instead of ice.

simulation (Fig. 2). Cold fluid (bright) unites more mass per volume and congregates into thin streaks that push downward through warmer surrounding fluid (dark). The lowermost point of the streaks is marked by a plumelike tip structure with vortices at their sides. Looking at the horizontal cross section, a honeycomb pattern is seen for both laboratory experiment and numerical simulation. From the comparison of vertical and horizontal cross sections, one observes that plumes actually form the septum of the honeycomb cells. Cold plumes push down along the cell rim while fluid must consequently move up in the interior of the cell. Plumes are the dominant structures. Their movement and diffusive decay mixes the water beneath the ice in the so-called mixed layer. The mixing successively entrains calm, warmer water from below and the colder mixed layer broadens. Both laboratory experiments and simulations exhibit this working principle, known from the convective boundary layer (CBL) in the atmosphere (Stull 1988), but vertically inverted, and from Rayleigh–Bénard convection (Chillá and Schumacher 2012).

Quantitatively, the time evolution of temperature profiles of individual laboratory realizations, as well as that of individual tower data from the simulation, varies strongly among each other. Hence, we draw the comparison on the

basis of the mean-temperature profiles instead of on the basis of individual laboratory realizations and individual tower data from the simulation.

The mean profiles evolve as described in the previous paragraph: a mixed layer develops and broadens in time. The broadening happens at the same pace in the laboratory experiment as in the simulation (not shown) and takes about 7 min to cover a height of  $0.40h_{\text{water}}$ , with the tank height  $h_{\text{water}} = 0.347$  m. In the mixed layer, we find a mean temperature almost constant in time. At the interface, the mean normalized temperature decreases by an order of magnitude over a distance of  $\sim 0.05h_{\text{water}}$  for both laboratory and simulation. This region forms part of what is generally referred to as “the surface layer” (Stull 1988).

Differences between the laboratory experiment and simulation exist in the boundary conditions, the initial conditions, and the system itself. Moreover the presence of the measuring device alters the flow. We hence expect some differences between the laboratory experiment and the numerical simulations but find that such differences are statistically insignificant.

To show this, we perform a Kolmogorov–Smirnov test on the mean profiles with the following null hypothesis: the laboratory measurements and simulation tower data

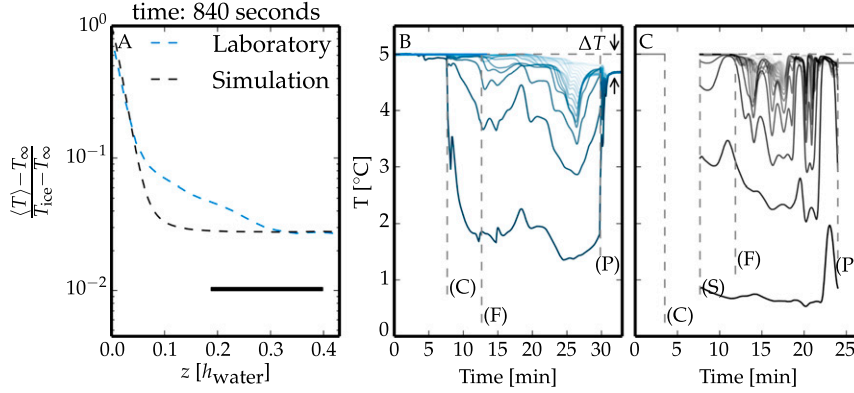


FIG. 3. Comparison of laboratory (blue) and simulation (black) temperature profiles. (a) The laboratory temperature profile (blue dashed line) is averaged over 25 realizations of  $T_\infty = 5^{\circ}\text{C}$  after equal elapsing times of 14 min. The simulation temperature profile (black dashed line) is obtained from a horizontal average. The black bar below the profiles indicates the region of quantitative agreement between laboratory experiment and simulation. In these regions we cannot reject the null hypothesis that the laboratory ensemble members and the mean profile of the simulation are drawn from the same distribution according to a Kolmogorov–Smirnov test. (b) Temporal evolution of one realization of a temperature-profile measurement taken from the laboratory. Intense colors mark thermistors next to the interface; light colors mark thermistors further away. C marks the time of ice–water contact, F marks the time when turbulence approximately sets in, and P marks the time of external mixing with a pump. After P, we find a temperature difference  $T_\infty - T_{\text{end}}$  of the averaged mean-temperature profile with respect to the temperature prior to the experimental conduct. (c) As in (b), taken from the simulation. S marks the starting time of the simulation.

are drawn from the same distribution. We cannot reject the null hypothesis on a significance level of 5% for the regions indicated by the gray bars in Fig. 3a. The laboratory measurement and tower data are thus to be considered as statistically equivalent in those regions. The regions broaden with evolving time and stretch from close to the interface to roughly half of the mixed layer.

In summary, we find qualitative and quantitative agreement between the simulation and laboratory experiment for the given number of laboratory realizations. Both experiments and simulations are used in the following section to investigate the melt rate of the ice.

#### 4. The melt rate

Ice melts if more internal energy per area and time  $H_{\text{water}}$  is supplied to the ice interface than can be transported away ( $H_{\text{ice}}$ ). We focus on an isothermal ice block with  $H_{\text{ice}} = 0$ . Hence, the melt rate  $w_f$  is solely determined by  $H_{\text{water}}$ , according to

$$w_f = \frac{1}{\rho_{\text{ice}} L} H_{\text{water}}, \quad (8)$$

where  $L = 333.5 \text{ kJ kg}^{-1}$  is the specific energy required to melt the ice (Frankenstein and Garner 1967), and  $\rho_{\text{ice}} = 916.8 \text{ kg m}^{-3}$  is the density of pure ice at  $0^{\circ}\text{C}$

(Pounder 1965). The internal-energy flux at the ice interface  $H_{\text{water}}$  originates from the evolution of the internal energy in the fluid system. The mean evolution of the internal energy [Eq. (3c)] is

$$\partial_t \langle T \rangle(z, t) = -\frac{1}{\rho_{\text{water}} c_p} \partial_3 H(z, t), \quad (9)$$

with

$$H(z, t) = -\rho_{\text{water}} c_p [\kappa \partial_3 \langle T \rangle(z, t) - \langle v_3 T' \rangle(z, t)]. \quad (10)$$

The specific heat capacity of water is  $c_p = 4.22 \text{ kJ kg}^{-1} \text{ K}^{-1}$ , the thermal diffusivity of water is  $\kappa = 1.36 \times 10^{-7} \text{ m}^2 \text{ s}^{-1}$  at  $273.15 \text{ K}$  (Sharqawy et al. 2010) and  $\rho_{\text{water}} = \rho(T_\infty)$ .

##### a. Melt rates observed in the laboratory experiment

In the laboratory experiments, we estimate the energy fluxes and the melt rates [Eq. (8)] from the net change of the internal energy  $\Delta E_{\text{int}} = m_{\text{water}} c_p (T_{\text{end}} - T_\infty)$  over the experiment run time  $t_{\text{run}}$ . After the run time  $t_{\text{run}}$ , the initial mean bulk temperature  $T_\infty$  has decreased to its final value  $T_{\text{end}}$ . The net change of the internal energy  $\Delta E_{\text{int}}$  is converted to the heat of fusion  $m_{\text{ice}} L$  and to internal energy of the meltwater  $m_{\text{ice}} c_p (T_{\text{end}} - T_{\text{ice}})$ . From the integral formulation of Eq. (9) one obtains the internal-energy balance of the system:

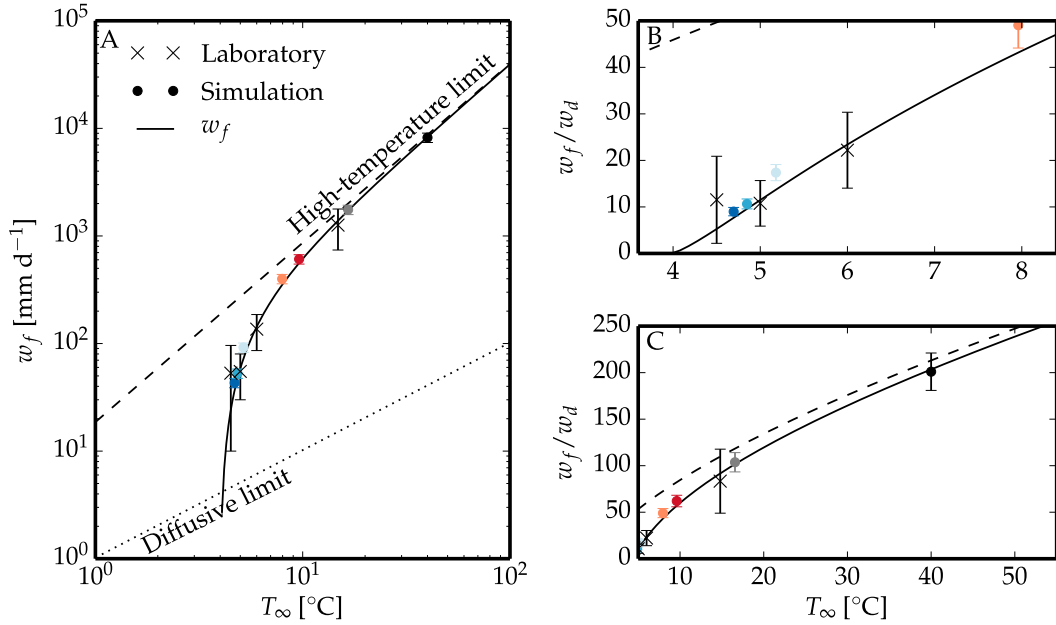


FIG. 4. Melt rate derived from a scalar gradient at the interface (simulation, colored dots corresponding to Fig. 1) and derived from bulk temperature change (laboratory, crosses). Analytical melt rate  $w_f$ , as given in Eq. (21) (black solid line). Diffusive melt rates  $w_d$ , as given in Eq. (13) (dotted line). The dashed line indicates the high temperature melt-rate limit. The black dot represents the simulation  $\theta_m = 1$  that does not have a stable stratification next to the interface. This simulation is exemplarily provided for a far-field temperature of  $T_\infty = 40^\circ\text{C}$ . (a) Double logarithmic plot illustrates the power-law change over the full temperature range. (b) Linear plot illustrates the melt-rate enhancement in the low-temperature range. (c) As in (b), but for the high-temperature range.

$$m_{\text{water}} c_p (T_{\text{end}} - T_\infty) = m_{\text{ice}} L + m_{\text{ice}} c_p (T_{\text{end}} - T_{\text{ice}}), \quad (11)$$

where  $m_{\text{ice}}$  is the mass of the melted ice, and  $m_{\text{water}}$  is the mass of the water in the tank.

Equation (11) assumes that no energy flows through water body boundaries except through the ice–water interface. To test this assumption, we estimate the mean energy flow through water-body boundaries other than the ice–water interface from time series of the bulk water temperature without ice attached on the water. We find a relative uncertainty in  $\Delta E_{\text{int}}$  due to all neglected mean energy fluxes of about 15%.

From Eq. (11), from the approximation that water and ice share the same base area  $A$ , from  $m_{\text{ice}} = \rho_{\text{ice}} h_{\text{ice}} A$  and from  $m_{\text{water}} = \rho_{\text{water}} h_{\text{water}} A$ , the height  $h_{\text{ice}}$  of the melted ice is given as

$$h_{\text{ice}} = h_{\text{water}} \frac{\rho_{\text{water}}}{\rho_{\text{ice}}} \frac{c_p (T_\infty - T_{\text{end}})}{L + c_p (T_{\text{end}} - T_{\text{ice}})}. \quad (12)$$

Several laboratory experiments for the same temperature  $T_\infty$ , but with different run time  $t_{\text{run}}$ , allow us to estimate a melt rate  $w_f = \Delta h_{\text{ice}} / \Delta t_{\text{run}}$  from the data. This assumes a constant energy flux at the interface, which is the leading-order behavior for free-convection systems

and which we observe for all our simulations (presented in section 4c). The standard deviation among the calculated heights at each  $t_{\text{run}}$  is less than 13%. We obtain the melt rates  $w_f = [53, 55, 136, 1260] \text{ mm day}^{-1}$  for  $T_\infty = [4.5, 5, 6, 14.8]^\circ\text{C}$  within the error bounds supplied in Fig. 4 (crosses and black solid bars). We compare these melt rates  $w_f$  to the melt rates  $w_d$  of a purely diffusive experiment that has a similar boundary layer extent. To allow for such comparison, we need an expression that describes how the melt  $w_d$  depends on boundary layer extent, which can be obtained from the derivative of a diffusive temperature profile  $T_d(z)$ :

$$\begin{aligned} w_d &= -\frac{\rho_{\text{water}}}{\rho_{\text{ice}}} \frac{c_p}{L} \kappa \partial_3 \langle T_d \rangle|_\delta \\ &= -\frac{\rho_{\text{water}}}{\rho_{\text{ice}}} \frac{c_p \Delta T_\infty}{L} \frac{\kappa}{\delta} \left[ \frac{2 \operatorname{erf}^{-1}(-.995)}{\sqrt{\pi}} \right], \end{aligned} \quad (13)$$

where  $T_d(z)$  is assumed to be an error function, a solution of the diffusion equation for the Dirichlet boundary conditions  $T_d(z=0) = T_{\text{ice}}$  and  $T_d(z \rightarrow \infty) = T_\infty$ . The boundary layer height  $\delta$  is defined based on the threshold criterion  $[\langle T_d(z=\delta) \rangle - T_{\text{ice}}] / \Delta T_\infty = 0.995$ . In the following, we choose  $\delta = h_{\text{water}}$ , so that  $w_d$  represents

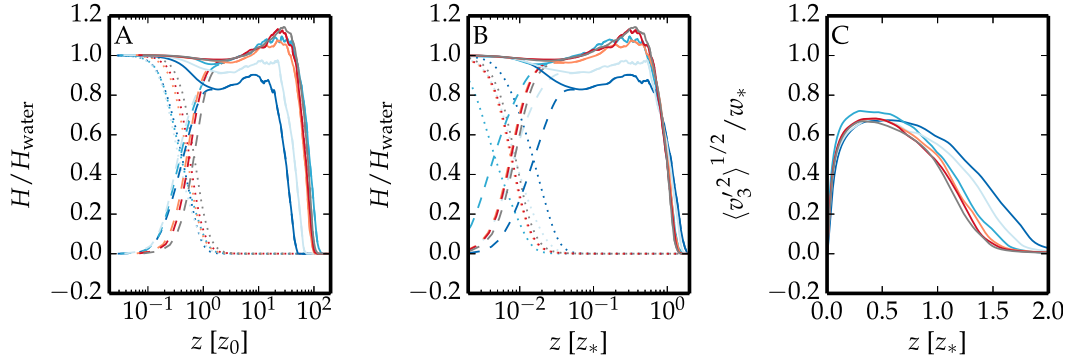


FIG. 5. Simulation internal-energy flux and velocity fluctuation at final simulation time. Colors indicate different far-field temperatures according to Fig. 1. Molecular (dotted) and turbulent (dashed) fluxes contribute to the total internal-energy flux (solid). (a) Internal-energy flux with abscissa normalized by the diffusive scale. (b) Internal-energy flux with abscissa normalized by the convective scale. (c) Vertical velocity fluctuation, normalized by the convective scale.

melt rates of diffusive experiments of the size of the laboratory tank.

We find that for the same boundary layer extent, the melt rates  $w_f$  are increased by one to two orders of magnitude compared to  $w_d$  (Figs. 4b,c), in contrast to the increase by a constant factor of about 2.5 reported in Martin and Kauffman (1977). We will elaborate on this finding in section 5a.

#### b. Melt rates simulated in the numerical experiment

In the simulation, we evaluate the melt rates from the horizontally averaged energy flux  $H_{\text{water}}$  according to Eqs. (8) and (10). At the interface ( $z = 0$ ) one finds

$$H_{\text{water}} \equiv H(z, t)|_{z=0} = -\rho_{\text{water}} c_p \kappa \partial_3 \langle T \rangle. \quad (14)$$

We obtain melt rates for several simulations of varying far-field temperature (Table 1, Fig. 4a, dots). We can infer two important results: First, the melt rates of the simulations and of the laboratory experiments match within the limits of their respective uncertainties. [The relative error of the melt rates from the simulation is less than 10% due to varying initial conditions (Mellado 2012).] Second, the melt rates depend strongly on the far-field temperature. From temperatures  $T_\infty = 3.98^\circ\text{C}$  to  $T_\infty = 5.20^\circ\text{C}$ , melt rates increase strongly from diffusive values of  $11 \text{ mm day}^{-1}$  (dashed line) up to  $86 \text{ mm d}^{-1}$  (Fig. 4b, blue dot), that is, a factor of  $\approx 8$ . From temperatures of  $T_\infty = 17^\circ\text{C}$  to  $T_\infty = 40^\circ\text{C}$ , melt rates increase from  $1.7$  to  $7 \text{ m day}^{-1}$  (Fig. 4c, gray dot and plus), that is, a factor of  $\approx 4$ .

The simulation of  $\theta_m = 1$  cannot be assigned to a definite far-field temperature;  $\theta_m = 1$  is the limit of high far-field temperatures [Eq. (7)] and of negligible buoyancy reversal. For this simulation, we find the minimum buoyancy directly at the wall (Fig. 1d, dashed line). This

situation is reminiscent of the free convection over a heated plate (Mellado 2012), where buoyancy increases linearly with the stratifying agent from the minimum value at the wall to the far field. We provide the melt rate derived from our simulation of  $\theta_m = 1$  exemplarily for a far-field temperature of  $T_\infty = 40^\circ\text{C}$ , for which we expect the assumption of negligible buoyancy reversal to be a sufficiently good approximation (Fig. 4, plus).

## 5. The energy flux and the flow structure

The partitioning of the internal-energy flux according to Eq. (10) into a molecular flux  $-c_p \rho \kappa \partial_3 \langle T \rangle$  and a turbulent flux  $c_p \rho \langle v_3' T' \rangle$  further confirms the working principle described in section 3; the positive turbulent flux, plotted in Fig. 5, shows that negative temperature fluctuations occur with descending motion, and positive temperature fluctuations occur together with ascending motion in most of the domain (dashed line). In other words, cold water descends, warm water ascends. At the interface, the no penetration condition suppresses the turbulent flux, and the molecular flux remains as the only transport mechanism (dotted line). The total energy flux (solid) is sustained by turbulent entrainment of warm far-field water at the lower boundary of the mixed layer. As the mixed layer broadens with time, it entrains warm water at a rate that yields a spatially constant energy flux throughout the mixed layer (solid line). The energy flux throughout the system determines the energy flux at the interface  $H_{\text{water}}$ . The constant flux foretells, according to Eq. (9), a steady mean-temperature profile despite cooling from the interface. A large extent of the system is hence in dynamic equilibrium (Mellado 2012). As a consequence, we expect a steady temperature gradient at the interface, that is, a constant melt rate.

The illustrated working principle and the internal-energy flux partition warrant a separate description of the diffusion-dominated inner layer and the turbulence-dominated mixed layer.

### a. The diffusion-dominated inner layer

Next to the interface, the normalized temperature changes by an order of magnitude over a diffusion-dominated layer of thickness  $z_0$ . The layer is stably stratified except for an unstably stratified fraction at its lower bound. This unstable fraction tends to overturn and hence tends to thin the diffusion-dominated layer. Such a situation is reminiscent of the buoyancy-reversal configuration studied, for example, by [Siems et al. \(1990\)](#) and [Mellado \(2010\)](#). The overturning fraction covers the normalized-temperature range  $[0, 2\theta_m]$  [Eq. (4) and Fig. 1d] and thus extends over a distance  $2\theta_m z_0$ . A buoyancy perturbation within  $2\theta_m z_0$  accelerates the flow proportionally to  $b_m$ , whereas the viscosity decelerates the flow proportionally to  $\nu$ . The time scale of the perturbation growth is  $t_{\text{buoy}} = (\nu/b_m)/(2\theta_m z_0)$  ([Turner 1973](#)). On the other hand, diffusion broadens  $z_0$  at a rate  $\kappa/z_0$ . The time scale of diffusive advancement over the overturning fraction  $2\theta_m z_0$  is hence  $t_{\text{diff}} = (2\theta_m z_0)/(\kappa/z_0)$ . While the diffusive advancement increases  $z_0$ , the buoyancy perturbation accelerates fluid away from the region and decreases  $z_0$ . The critical depth at which the rate of thinning is equal to the rate of broadening,  $t_{\text{diff}} = t_{\text{buoy}}$ , marks the extent of the diffusion-dominated layer  $z_0$ :

$$z_0 = \frac{10}{(2\theta_m)^{2/3}} \text{Pr}^{1/3} (\kappa^2/b_m)^{1/3}. \quad (15)$$

The layer of depth  $z_0$  is “the diffusive sublayer,” a part of the surface layer that has been introduced in the previous section. The factor 10 gives the commonly used criticality for this Rayleigh number criterion. The depth  $z_0$  is independent of time; the diffusive sublayer has a fixed extent.

### b. The turbulence-dominated mixed layer

The mixed layer, on the contrary, is unsteady; it broadens in time. Still, some statistical properties behave self-similarly when normalized with a boundary layer height

$$z_* = \frac{1}{H_{\text{water}}} \int_0^\infty \mathcal{H}(\langle T'v'_3 \rangle) \langle T'v'_3 \rangle dz \quad (16)$$

(Fig. 5b) and a convective velocity scale

$$w_*^3 = \int_0^\infty \mathcal{H}(\langle b'v'_3 \rangle) \langle b'v'_3 \rangle dz \quad (17)$$

(Fig. 5c), where  $\mathcal{H}$  is the Heaviside function. This expression for the convective velocity scale  $w_*$  is obtained

from the inviscid scaling of the viscous dissipation rate  $\varepsilon \propto w_*^3 z_*^{-1}$  ([Pope 2000](#)) and the observation that

$$\frac{\int_0^\infty \varepsilon dz}{\int_0^\infty \langle b'v'_3 \rangle dz} \approx 0.7 \quad (18)$$

in our simulations. This result implies that the viscous dissipation rate  $\varepsilon$  balances a large constant fraction of the turbulent buoyancy production  $\langle b'v'_3 \rangle$ .

### c. The energy flux of fully developed systems

After an initial transient, the energy flux of all simulations decays toward a constant value (Fig. 6). The warmer the far-field water is, the larger the energy flux. The energy flux in terms of the temperature gradient ranges over more than one order of magnitude, from  $2.6 \times 10^2 \text{ K m}^{-1}$  at  $T_\infty \approx 4.8^\circ\text{C}$  to  $3.7 \times 10^3 \text{ K m}^{-1}$  at  $T_\infty = 9.6^\circ\text{C}$ . Much of this dependence on  $T_\infty$  can be explained from the previous analysis of the diffusion-dominated inner layer. From this analysis, we know that this gradient is described to first order by a temperature drop of  $\Delta T_\infty$  over a length  $z_0$ :

$$\partial_3 \langle T \rangle(z, t)|_{z=0} = f(\theta_m) \Delta T_\infty z_0^{-1}, \quad (19)$$

with the proportionality constant  $f$  only dependent on the far-field temperature parameter  $\theta_m$ . [Figure 6b](#) confirms this estimate, although  $f$  still varies within the interval  $[1, 0; 2, 2]$ .

So far, the diffusive length scale  $z_0$  has been derived as the critical depth at which molecular diffusion and buoyancy are in balance. This reasoning was inspired by the analogy between this study and the cloud-top mixing layer. The system in this study, however, has a solid wall next to the diffusive sublayer. Hence, we attribute the variation  $f$  of the normalized temperature gradient at the wall (Fig. 6) to the presence of the wall. In the absence of a theoretical description of the influence of the wall, we suggest accounting for it by an empirical first guess:

$$f(\theta_m) = 2 - \theta_m \quad (20)$$

(Fig. 6, dotted line).

## 6. The melt rate as a function of the far-field temperature

The previous results are now combined to give an analytical expression for the melt rate of a thermally driven fresh-ice–freshwater interface for  $\Delta T_\infty > \Delta T_m$ . Substituting the definition of  $z_0$  [Eq. (15)] into the flux

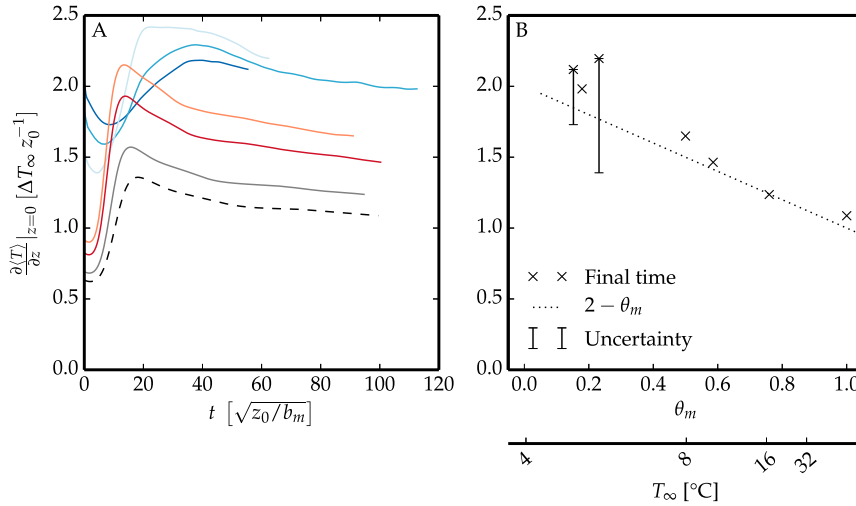


FIG. 6. Melt rates given as the interfacial temperature gradient in units of  $\Delta T_\infty/z_0$ . (a) All simulations seem to approach a normalized temperature gradient between one and two. Colors indicate different far-field temperatures according to Fig. 1. (b) Temperature gradient at final simulation time over the far-field temperature parameter  $\theta_m$ , defined in Eq. (7), and  $f(\theta_m)$  (dotted line).

parameterization [Eq. (19)], the melt rate, given by Eqs. (8) and (14), can be written as

$$w_f = w_{f,0} \left[ \frac{(T_\infty - T_m)^2}{\Delta T_\infty \Delta T_m} \right]^{2/3} \left( \frac{\Delta T_\infty + \Delta T_m}{\Delta T_m} \right), \quad (21)$$

where Eqs. (5), (7), and (20) have been used to express the dependency in terms of  $T_\infty$  instead of  $\theta_m$ . The pre-factor is

$$w_{f,0} = \left( \frac{2^2}{10^3 \text{Pr}} \right)^{1/3} \frac{\rho_{\text{water}}}{\rho_{\text{ice}}} \frac{c_p \Delta T_m}{L} \left( g \frac{\beta T_m^2 \kappa}{\rho_{\text{water}}} \right)^{1/3} = 2.15 \times 10^{-6} \text{ m s}^{-1}, \quad (22)$$

with  $\text{Pr} = 10$  (Fig. 4, black solid line). The term  $w_{f,0}$  corresponds to  $1.86 \times 10^2 \text{ mm day}^{-1}$ . Note that in nature  $\text{Pr} = \text{Pr}(T)$  and varies from 13.18 to 5.40 in the relevant temperature range of  $0^\circ$  to  $30^\circ\text{C}$  (Sharqawy et al. 2010). The melt rates of Eq. (21) match the melt rates estimated in the laboratory experiment and in the simulations. Equation (21) seems to slightly underestimate the simulation results for low far-field temperatures (Fig. 4b), but not all these simulations have yet completely reached their steady behavior.

The enhancement of the melt rate  $w_f/w_d$  increases by a factor of 40 as the far-field temperature increases from  $4^\circ$  and  $8^\circ\text{C}$  (Fig. 4b). The enhancement of the melt rate increases by a factor of about 1.5 as the far-field temperature increases from  $20^\circ$  to  $40^\circ\text{C}$  (Fig. 4c). Thus, the relative enhancement of the melt rates with far-field temperature decreases for increasing temperature.

The comparison of Eq. (21) to the corresponding expression of free convection without buoyancy reversal reveals the dynamics of the system. With Eqs. (5), (8), and (14) and the diffusive length scale in free convection without buoyancy reversal,  $z_{\text{diff}} = (\kappa^2/b_m)^{1/3}$ , one finds

$$w_f \propto \left( \frac{T_\infty - T_m}{\Delta T_m} \right)^{2/3} \frac{\Delta T_\infty}{\Delta T_m}. \quad (23)$$

In the high temperature limit,  $(T_\infty - T_m)/\Delta T_m \gg 1$ , we obtain  $(\Delta T_\infty/\Delta T_m)^{5/3}$  from Eq. (23), and we also obtain  $(\Delta T_\infty/\Delta T_m)^{5/3}$  from Eq. (21) (Fig. 4, dashed line). Thus, the high temperature limit of Eq. (21) corresponds to the behavior found for the heated plate, where no stable stratification is present. We conclude that the shielding of the interface by the stable stratification next to it effectively vanishes for  $T_\infty \gg T_m$ .

In the low temperature limit,  $(T_\infty - T_m)/\Delta T_m < 1$ , we obtain  $[(T_\infty - T_m)/\Delta T_m]^{2/3}$  from Eq. (23) in contrast to  $[(T_\infty - T_m)/\Delta T_m]^{4/3}$  from Eq. (21). Thus, the shielding of the interface—incorporated in Eq. (21) but not in Eq. (23)—diminishes the melt rate by a power of two if it is expressed as a function of the relative temperature difference  $(\Delta T_\infty - \Delta T_m)/\Delta T_m < 1$ .

## 7. Discussion

### a. The influence of meltwater on the melt rate

When ice melts, it forms meltwater of  $T = 0^\circ\text{C}$ . Recently formed meltwater does not possess any kinetic energy and thickens the diffusive sublayer in which the

stable stratification occurs. Thus, meltwater increases the shielding of the ice from rising warm fluid and diminishes the melt rate. This describes a negative feedback. We now assess its strength.

In a frame of reference that moves with an interface melting at speed  $w_{\text{ice}}$ , the formation of meltwater appears as vertical background mean advection. The corresponding advection velocity is

$$v_{\text{int}} = -\frac{\rho_{\text{ice}}}{\rho_{\text{water}}} w_{\text{ice}}. \quad (24)$$

In principle,  $w_{\text{ice}}$  depends on time and on the position within the interface. We have seen already that the time dependence of the mean value vanishes after an initial transient, when the system is freely developing (Fig. 6). For now, we also assume no dependence on the position within the interface, but we will assess this assumption in the next section.

With constant  $v_{\text{int}}$ , the moving frame of reference is still an inertial system. The governing Eqs. (3) still apply, but different boundary conditions need to be considered. Instead of no-slip, no penetration boundary conditions, the system imposes no-slip, constant velocity boundary conditions  $v_i(z=0) = v_{\text{int}}\delta_{i3}$ .

We obtain an estimate for the influence of the constant-velocity boundary condition on the melt rate from the comparison of the advection to the diffusion flux at the interface using  $w_{\text{ice}} = w_f$  in Eq. (24):

$$\frac{v_{\text{int}}(T_{\text{ice}} - T_{\infty})}{\kappa\partial_3(T)|_{z=0}} = \frac{v_{\text{int}}(T_{\text{ice}} - T_{\infty})}{(L/c_p)v_{\text{int}}} = \frac{c_p}{L}(T_{\text{ice}} - T_{\infty}). \quad (25)$$

For far-field temperatures approaching  $T_m$ , the estimate approaches  $(c_p/L)(T_{\text{ice}} - T_m) \approx 1/20$  and diverges for high far-field temperatures (Fig. 7, line). The divergence for high far-field temperatures exposes that the estimate of Eq. (25) does not account for the full feedback mechanism described above. Meltwater cannot diminish the melt rate infinitely but only diminishes it as long as ice is melting. Here, we only considered a fixed constant velocity boundary condition with  $w_{\text{ice}}$  determined from Eq. (21). So Eq. (25) is merely a maximum estimator to the feedback mechanism, and we expect to find a smaller diminution in practice than estimated here.

To verify these estimates, we conduct a set of three simulations at temperatures  $T_{\infty} \in \{8, 25, 40\}^{\circ}\text{C}$  that account for the meltwater formation with  $v_{\text{int}}$  set accordingly. We compare the melt rates of these simulations  $\tilde{w}_f$  to the analytical melt rate  $w_f$  obtained from Eq. (21) as  $(\tilde{w}_f - w_f)w_f^{-1}$ . The values range within those of the analytical maximum estimator [Eq. (25)] and confirm the diminishing effect of meltwater on  $w_f(T_{\infty})$  (Fig. 7,

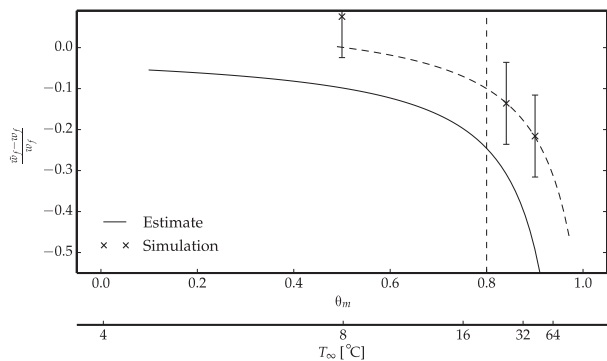


FIG. 7. Estimates of the influence of meltwater formation at the interface on the melt rate. (black) Analytical estimate [Eq. (25)]. (crosses) Numerical estimate derived from comparison between analytical melt rates and melt rates obtained from simulations with background mean advection. (dashed lines) Guidelines for the eye.

dashed line). The simulated diminution and Eq. (25) follow a similar dependence on  $T_{\infty}$ , with an offset of  $\approx -8\%$  and a shift of  $\approx 0.06\theta_m$ . Hence, the velocity  $v_{\text{int}}$  of each of the three simulations was systematically chosen too high to correctly represent reality. Smaller velocities  $v_{\text{int}}$  would in fact diminish the melt rate less and yield melt rates closer to Eq. (21).

We find the numerical estimate in agreement with the laboratory experiments. We did not observe a pronounced signature of the meltwater in the flow structure as compared to the simulations with no penetration boundary conditions.

We conclude that the effect of meltwater formation can at least be neglected for far-field temperatures  $T_{\infty} < 20^{\circ}\text{C}$  ( $\theta_m = 0.8$ ). Within this limit the presented melt-rate equation [Eq. (21)] holds with a diminution of less than 10% due to the influence of meltwater (Fig. 7, black dashed lines). For far-field temperatures  $T_{\infty} \gg 20^{\circ}\text{C}$ , for which the influence of the meltwater is significant, we expect the feedback to yield a temperature dependence in between  $w_f \propto \Delta T_{\infty}$  (diffusive) and  $w_f \propto \Delta T_{\infty}^{5/3}$  (turbulent).

### b. Spatial inhomogeneity of the melt rate

The temperature gradient at the interface (Figs. 8a,b) varies in space  $(x_1, x_2)$ . We now assess this variation of the melt rate around its mean value [Eq. (21)] on the basis of the probability density function (pdf; Fig. 8c).

The ensemble of pdfs for different far-field temperatures exhibits two main modes of different characteristic. The first mode is dominant in pdfs of low far-field temperatures, represents melt rates smaller than the mean, and has a relative standard deviation of 10%. The second mode is dominant in pdfs of high far-field temperatures, represents the mean, and has a relative

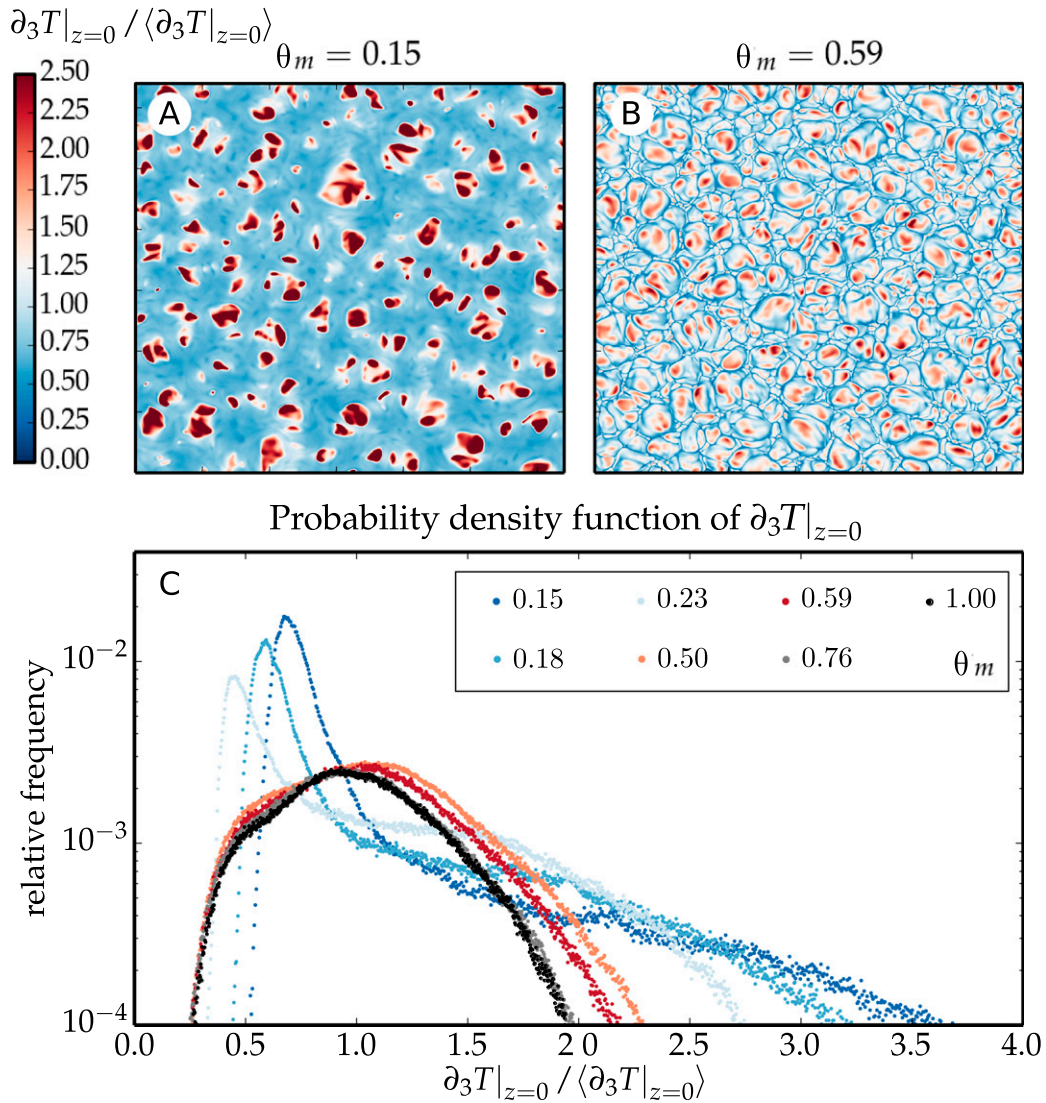


FIG. 8. Dependence of the melt rate on the position within the interface  $[\partial_3 T|_{z=0}(x_1, x_2) / \langle \partial_3 T|_{z=0} \rangle]$  for (a)  $\theta_m = 0.15$ , and (b)  $\theta_m = 0.59$ . (c) Probability density function of  $\partial_3 T|_{z=0} / \langle \partial_3 T|_{z=0} \rangle$ .

standard deviation of 60%. In the diffusive limit, that is in the absence of convection, one expects to find a pdf that is a delta function at  $\langle \partial_3 T|_{z=0} \rangle$ . The first mode is considerably narrower than the second mode and yields absolute melt rates close to those of purely diffusive melting (Fig. 4). We refer to the first mode as the diffusive mode. The second mode at the center of the pdf resembles the melt rate in the high temperature limit  $\theta_m = 1$  (Fig. 1d, dashed curve; cf. Fig. 8c, black). This mode is purely convection dominated, as can be inferred from the interface pattern (Fig. 8b). We refer to the second mode as the turbulent mode.

With increasing far-field temperature, we observe a shift of the main contribution to the pdf from the

diffusive mode to the turbulent mode. This transition is in line with the mechanism proposed so far; for low far-field temperatures, a strong stable stratification close to the interface shields the ice from the rising warm turbulent water. Only a few rising plumes manage to intrude this shield and enhance the melting at the interface locally (Fig. 8a). This local turbulent intrusion contributes to the pdf at values of up to several times larger than the first mode. For high far-field temperatures, the strength of the stable stratification is not sufficient to shield the ice anymore. The increasing contribution of the turbulent mode broadens the absolute bandwidth of the pdf (not shown) and shifts the diffusive mode to lower relative values. As the importance of the diffusive

mode ceases, the relative bandwidth of the pdf reduces. Then, the ice is immediately exposed to rising, warm turbulent plumes, and we find an interface pattern known from the turbulent free-convective motion (Fig. 8b).

We found in the last section that the influence of the meltwater formation is negligible for low far-field temperatures. For increasing far-field temperatures, the shielding effect of the meltwater becomes more relevant, according to Eq. (25). Based on this result, we can infer that the maintenance of a spatially resolved  $v_{\text{int}}(x_1, x_2)$  in section 7a would diminish the high temperature end of the pdf more than it would diminish the low temperature end of the pdf. This would homogenize the interface pattern found in Fig. 8b and would narrow the bandwidth of the probability density function in Fig. 8c.

### c. Application of this work to the ice–ocean interface

The motivation to study the present setup has been its structural similarity to the sea-ice–ocean interface and to the ice-shelf–ocean interface. The question arises of how much information can be transferred from our findings to such interfaces. We are aware that ice–ocean interfaces do not just melt but ablate in the interplay of differently diffusing salinity and temperature. Still, we use our model as a simplified approach and focus only on the shape of the mean-buoyancy profile.

The process-based analysis, used to derive the scaling laws of the inner layer, suggests that the strength of the stable-stratification shield beneath the ice characterizes the flow. The stable stratification has shown to shield the ice for all  $b(z=0) > b_m$ . We define the relative strength of the shielding as the strength of the stable stratification  $\Delta b = b(z=0) - b_m$  compared to the strength of the buoyancy forcing  $b_m$  (Fig. 1d). This is effectively the Richardson number

$$\text{Ri}_0 = \frac{\Delta b z_0}{w_0^2} = \frac{\Delta b z_0}{|b_m| z_0} = \frac{b(z=0)}{|b_m|} + 1 \quad (26)$$

that describes the ratio between the potential energy that a fluid particle requires in order to overcome the diffusive shield  $\Delta b$  of thickness  $z_0$  and the kinetic energy  $w_0^2$  that a fluid particle acquires in free fall with an acceleration  $b_m$  over a distance  $z_0$ .

Martin and Kauffman (1977) study the case of the sea-ice–ocean interface in a laboratory tank experiment. We derive  $b(z=0) \approx 0.1385 \text{ m s}^{-2}$  from their salinity and temperature profiles given in Fig. 2e and Eq. (9) of their study together with Eq. (1) of this study. (The zero-order density is taken as  $10^3 \text{ kg m}^{-3}$  and not as  $10^2 \text{ kg m}^{-3}$  as given in their study.) With a redefinition of the minimum buoyancy that accounts for the influence of temperature and salinity,

$$b_m = g \frac{\rho(S_\infty, T_{\text{ice}}) - \rho(S_\infty, T_\infty)}{\rho(S_\infty, T_\infty)}, \quad (27)$$

using the far-field salinity  $S_\infty$  taken from their salinity profile, we find  $b_m \approx 0.0011 \text{ m s}^{-2}$  and  $\text{Ri}_0 \approx 129$ . If we use the boundary conditions  $T_{\text{ice}}$ ,  $S_\infty$ , and  $T_\infty$  as provided from their one-dimensional theoretical model, we consistently obtain  $\text{Ri}_0 \approx 136$  for their setup. In the case studied in this work, we find a similarly strong stable stratification for a far-field temperature of  $T_\infty = 4.33^\circ\text{C}$ .

According to our results, turbulence enhances the melt rate by a factor  $w_f(T_\infty = 4.33^\circ\text{C})/w_d(T_\infty = 4.33^\circ\text{C}) \approx 3.1$ . Martin and Kauffman (1977) determined an enhancement of the melt rate by a constant factor of about 2.5. Given that we consider melt-rate variations over two orders of magnitude (Fig. 9a), this is in fairly good agreement despite the neglect of the influence of salt.

As opposed to the finding of Martin and Kauffman (1977), we find that turbulence does not enhance the melt rate by a constant factor, but by a factor that depends on the relative strength of the shielding, the Richardson number  $\text{Ri}_0$ . With the parameter range of far-field temperature and salinity that they provide from their model (Fig. 9, therein),  $\text{Ri}_0$  varies between  $10^2$  and  $10^3$  in their study. This order-of-magnitude variation in  $\text{Ri}_0$  translates to a variation in the turbulent enhancement  $w_f/w_d$  by a factor of approximately 4 according to Fig. 9a (herein). For  $T_\infty \in [10, 30]^\circ\text{C}$ ,  $\text{Ri}_0$  even yields  $O(10^1)$ ; the turbulent enhancement of the melt rate for  $\text{Ri}_0 = O(10^1)$  can be twice that of  $\text{Ri}_0 = 136$ . We conjecture that Martin and Kauffman (1977) would have found a turbulent enhancement of the melt rate by a factor of 5 for significantly increased far-field temperatures.

In nature, the flow beneath an ice interface is driven by several mechanisms. To allow for the comparison of our results to those of systems with different driving mechanisms, such as shear (McPhee 1983) or internal heating from radiation (Mironov et al. 2002), we propose to use the Richardson number

$$\text{Ri}_* = \frac{\Delta b z_0}{w_*^2} \quad (28)$$

instead of  $T_\infty$  as the independent variable. The direct link of the buoyancy-forcing strength  $b_m$  to the velocity scale of the system  $w_0$  is replaced by the more generic convective velocity scale of the system  $w_*$ , as defined in Eq. (17). The effect of  $T_\infty$  is still retained in  $\Delta b$ . This Richardson number describes the importance of the shielding by the diffusion-dominated, inner-layer relative to the specific kinetic energy contained in the

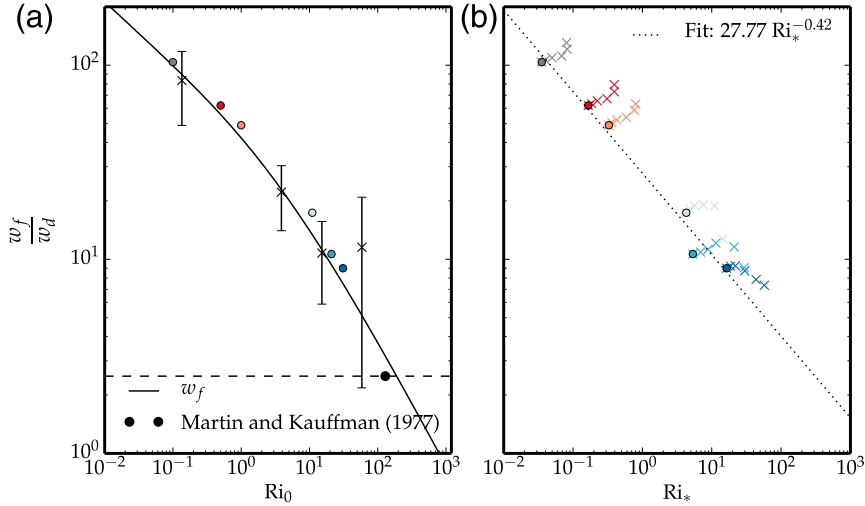


FIG. 9. Turbulent enhancement of the melt rate compared to the diffusive melt rate  $w_d$  [Eq. (13)] (a) over Richardson number  $Ri_0$  [Eq. (26)] with the simulations (dots), laboratory experiments of this study (crosses), Eq. (21) (solid), and the study of [Martin and Kauffman \(1977\)](#) (black dot: laboratory experiment, dashed line: one-dimensional theoretical model). Colors indicate different far-field temperatures according to [Fig. 1](#). (b) Turbulent enhancement of the melt rate over the Richardson number  $Ri_*$  [Eq. (29)]. Crosses indicate the temporal evolution toward the final simulation time (dots). The dotted line is a linear fit of the final simulation values  $\log(w_f/w_d)$  over  $\log(Ri_*)$ .

turbulence-dominated mixed layer ([Fernando and Hunt 1997](#)). One could thus interpret the simulations of different far-field temperatures as simulations of fixed far-field temperature but different  $Ri_*$  ([Fig. 9b](#)). From a linear fit of the final simulation values  $\log(w_f/w_d)$  over  $\log(Ri_*)$ , we conjecture that the melt rate follows  $Ri_*$  as

$$w_f \propto Ri_*^{-0.42}. \tag{29}$$

### 8. Conclusions

We have evaluated direct numerical simulations against laboratory experiments of turbulent convection beneath a horizontal ice–water interface. The structure of the flow differs insignificantly between the laboratory experiment and the simulations, and the melt rates agree quantitatively. We have thus complemented the temperature profile of the laboratory experiment with the temperature and flow fields of the simulation. Based on this data, we have derived, from first principles, an analytical expression for the melt rate of ice  $w_f$  under purely thermally driven conditions.

The simulations show that molecular diffusion sets and limits the energy exchange at the ice interface for all far-field temperatures. For far-field temperatures below 8°C, a stably stratified diffusive layer shields the ice from the turbulent outer layer. The thickness of the stably

stratified layer is  $z_0 \propto (\kappa^2/|b_m|)^{1/3}$ , with a buoyancy anomaly  $b_m = b(T = T_m)$ ,  $T_m = 3.98^\circ\text{C}$ , and buoyancy  $b$  defined with respect to the density in the far field. The flow structure is similar to that seen in cloud-top mixing layers. With increasing far-field temperature  $T_\infty$ , the stably stratified shield diminishes. For far-field temperatures far above 8°C, the stable stratification has effectively disappeared. Then the flow is similar to that found in free convection over a heated plate but upside down, with a diffusive layer thinner than the stably stratified diffusive layer.

The understanding of the flow structure is used to quantify the energy exchange at the ice–water interface. We provide in [Eq. \(21\)](#) an explicit parameterization of  $w_f$  that only depends on  $T_\infty$ , and we give  $w_f$  as a function of  $Ri_*$  in [Fig. 9b](#). The Richardson number  $Ri_* = \Delta b z_0 / w_*^2$  quantifies the strength of the stably stratified shield next to the ice with respect to the strength of turbulence. The buoyancy difference  $\Delta b = b(z = 0) - b_m$  is defined with the buoyancy at the interface  $b(z = 0)$ .

Based on the dependence of the melt rate on the far-field temperature  $T_\infty$ , three regimes can be distinguished: a linear dependence in the diffusive regime  $\Delta T_\infty < \Delta T_m$ , a dependence  $w_f \propto (T_\infty - T_m)^{5/3}$  in the high temperature limit  $T_\infty \gg 8^\circ\text{C}$ , and a dependence  $w_f \propto (T_\infty - T_m)^{4/3}$  in between. We find that the influence of meltwater on the melt rate can be neglected for far-field temperatures  $T_\infty < 20^\circ\text{C}$ .

In contrast to previous work, we find a turbulent enhancement of the melt rate by one to two orders of magnitude for a given boundary layer depth. Hence, our findings imply that turbulence needs to be considered in the analysis of ice–water dynamics even in shear-free conditions to obtain accurate ice-bottom melt rates.

*Acknowledgments.* We thank Alberto de Lozar and Cedrick Ansoorge for interesting discussions on the topic. Laboratory assistants involved in data acquisition were Simon Kamprath, Felix Matt, Thilo Klenz, and Niels Fuchs. We also acknowledge the support by the institute’s workshop and Leif Riemenschneider. Computational resources were supplied by Jülich Supercomputing Centre and German Climate Computing Centre. Primary data and scripts used in the analysis and other supplementary information that may be useful in reproducing the author’s work are archived by the Max Planck Institute for Meteorology and can be obtained by contacting publications@mpimet.mpg.de.

## APPENDIX

### The Effective Buoyancy Flux

Commonly, a relevant buoyancy flux scale of a free-convection system  $B_{\text{eff}}$  is known a priori and is then used in combination with the boundary layer height  $z_*$  to construct a velocity scale from  $(B_{\text{eff}}z_*)^{1/3}$  (Deardorff 1970). In this work, however, a relevant buoyancy flux scale is not known a priori, nor is it readily evident from the internal-energy flux  $H_{\text{water}}$  via a buoyancy parameter that relates temperature and buoyancy [Eq. (5)]. Hence, we define an effective buoyancy flux by

$$B_{\text{eff}} = \frac{w_*^3}{z_*}. \quad (\text{A1})$$

For researchers interested in similar systems, we document that  $B_{\text{eff}}$  ranges between 0.1 and 0.4 in units of the diffusion-dominated buoyancy flux of free-convection systems  $(b_m^4 \kappa)^{1/3}$ . As a function of  $\theta_m$ ,  $B_{\text{eff}}$  decreases by a factor of 4 from the low temperature range to the high temperature limit, and  $B_{\text{eff}}$  is found to be constant in time, once the mixed layer is developed.

By definition of Eq. (A1), the effective buoyancy flux relates to the energy flux  $H_{\text{water}}$  as

$$H_{\text{water}} = B_{\text{eff}} \frac{\int_0^\infty \mathcal{H}(\langle T'v'_3 \rangle) \langle T'v'_3 \rangle dz}{\int_0^\infty \mathcal{H}(\langle b'v'_3 \rangle) \langle b'v'_3 \rangle dz} \quad (\text{A2})$$

The linear relationship  $H_{\text{water}}/B_{\text{eff}} \approx 0.55\theta_m T_\infty/b_m$  is empirically determined. With Eqs. (5), (7), (A1), and (A2), it yields

$$H_{\text{water}} = \alpha_T \frac{w_*^3}{z_*} \frac{\Delta T_m}{\Delta T_\infty - \Delta T_m}, \quad \text{and} \quad (\text{A3a})$$

$$\alpha_T = 8.3 \times 10^9 \text{ W s}^3 \text{ m}^{-4}. \quad (\text{A3b})$$

The term  $H_{\text{water}}$  is thus obtainable for systems of known far-field temperature  $T_\infty$  once estimates for the boundary layer height  $z_*$  and the convective velocity  $w_*$  are provided.

## REFERENCES

- Chillá, F., and J. Schumacher, 2012: New perspectives in turbulent Rayleigh–Bénard convection. *Eur. Phys. J. E*, **35**, 58, doi:10.1140/epje/i2012-12058-1.
- Deardorff, J. W., 1970: Convective velocity and temperature scales for the unstable planetary boundary layer and for Rayleigh convection. *J. Atmos. Sci.*, **27**, 1211–1213, doi:10.1175/1520-0469(1970)027<1211:CVATSF>2.0.CO;2.
- Fernando, H. J. S., and J. C. R. Hunt, 1997: Turbulence, waves and mixing at shear-free density interfaces. Part 1. A theoretical model. *J. Fluid Mech.*, **347**, 197–234, doi:10.1017/S0022112097006514.
- Frankenstein, G., and R. Garner, 1967: Equations for determining the brine volume of sea ice from  $-0.5^\circ$  to  $-22.9^\circ\text{C}$ . *J. Glaciol.*, **6**, 943–944.
- Keitzl, T., D. Notz, and J.-P. Mellado, 2014: How fast does ice melt from below? *67th Annual Meeting of the American Physical Society Division of Fluid Dynamics*, Boston, MA, American Physical Society, V0020, doi:10.1103/APS.DFD.2014.GFM.V0020.
- Lele, S. K., 1992: Compact finite difference schemes with spectral-like resolution. *J. Comput. Phys.*, **103**, 16–42, doi:10.1016/0021-9991(92)90324-R.
- Martin, S., and P. Kauffman, 1977: An experimental and theoretical study of the turbulent and laminar convection generated under a horizontal ice sheet floating on warm salty water. *J. Phys. Oceanogr.*, **7**, 272–283, doi:10.1175/1520-0485(1977)007<0272:AEATSO>2.0.CO;2.
- McPhee, M. G., 1983: Turbulent heat and momentum transfer in the oceanic boundary layer under melting pack ice. *J. Geophys. Res.*, **88**, 2827–2835, doi:10.1029/JC088iC05p02827.
- Mellado, J. P., 2010: The evaporatively driven cloud-top mixing layer. *J. Fluid Mech.*, **660**, 5–36, doi:10.1017/S0022112010002831.
- , 2012: Direct numerical simulation of free convection over a heated plate. *J. Fluid Mech.*, **712**, 418–450, doi:10.1017/jfm.2012.428.
- , and C. Ansoorge, 2012: Factorization of the Fourier transform of the pressure-Poisson equation using finite differences in collocated grids. *Z. Angew. Math. Mech.*, **92**, 380–392, doi:10.1002/zamm.201100078.
- Mironov, D., A. Terzhevik, G. Kirillin, T. Jonas, J. Malm, and D. Farmer, 2002: Radiatively driven convection in ice-covered lakes: Observations, scaling, and a mixed layer model. *J. Geophys. Res.*, **107** (C4), doi:10.1029/2001JC000892.
- Notz, D., M. G. MCPhee, M. G. Worster, G. A. Maykut, K. H. Schlunzen, and H. Eicken, 2003: Impact of underwater-ice

- evolution on Arctic summer sea ice. *J. Geophys. Res.*, **108**, 3223, doi:10.1029/2001JC001173.
- Perovich, D. K., J. Richter-Menge, B. C. Elder, C. Polashenski, T. Arbetter, and O. Brennick, 2013: It is the North Pole: Sea ice observations at the North Pole Environmental Observatory. *2013 Fall Meeting*, San Francisco, California, Amer. Geophys. Union, Abstract 31, C31A-0621.
- Pope, S. B., 2000: *Turbulent Flows*. Cambridge University Press, 802 pp.
- Pounder, E. R., 1965: *The Physics of Ice*. Pergamon Press, 151 pp.
- Sharqawy, M. H., J. H. Lienhard, and S. M. Zubair, 2010: Thermophysical properties of seawater: A review of existing correlations and data. *Desalin. Water Treat.*, **16**, 354–380, doi:10.5004/dwt.2010.1079.
- Siems, S. T., C. S. Bretherton, M. B. Baker, S. Shy, and R. E. Breidenthal, 1990: Buoyancy reversal and cloud-top entrainment instability. *Quart. J. Roy. Meteor. Soc.*, **116**, 705–739, doi:10.1002/qj.49711649309.
- Stull, R. B., 1988: *An Introduction to Boundary Layer Meteorology*. Kluwer Academic Publishers, 666 pp.
- Turner, J. S., 1973: *Buoyancy Effects in Fluids*. Cambridge University Press, 367 pp.
- Williamson, J. H., 1980: Low-storage Runge-Kutta schemes. *J. Comput. Phys.*, **35**, 48–56, doi:10.1016/0021-9991(80)90033-9.
- Wouters, B., A. Martin-Español, V. Helm, T. Flament, J. M. van Wessem, S. R. M. Ligtenberg, M. R. van den Broeke, and J. L. Bamber, 2015: Dynamic thinning of glaciers on the southern Antarctic Peninsula. *Science*, **348**, 899–903, doi:10.1126/science.aaa5727.
- Wunsch, S., 2003: Stochastic simulations of buoyancy-reversal experiments. *Phys. Fluids*, **15**, 1442–1456, doi:10.1063/1.1572160.